Research Square

Preprints are preliminary reports that have not undergone peer review.
They should not be considered conclusive, used to inform clinical practice,
or referenced by the media as validated information.

# Electrospinning Preparation of TiO2 Fiber Membranes and the Enhancement of Photocatalytic Uranium Reduction Efficiency by One-Dimensional Morphology

**Yongshuang You**
Southwest University of Science and Technology
**Shuangyang Zhou**
Southwest University of Science and Technology
**Xianqing Chen**
Southwest University of Science and Technology
**Lisha Yang**
Southwest University of Science and Technology
**Yan Liu**
Southwest University of Science and Technology
**Xinke Dan**
Southwest University of Science and Technology
**Jiawei Tian**
Southwest University of Science and Technology
**Shuying Shi**
shishuying@swust.edu.cn
Southwest University of Science and Technology
**Jianwen Zhang**
Southwest University of Science and Technology
**Hao Deng**
Southwest University of Science and Technology

**Research Article**

**Keywords:** Electrospinning, TiO2 fiber membranes, photocatalytic, U(VI)

**Posted Date:** June 22nd, 2026

**DOI:** https://doi.org/10.21203/rs.3.rs-9965144/v1

**License:** This work is licensed under a Creative Commons Attribution 4.0 International License. Read Full License

**Additional Declarations:** No competing interests reported.

## Abstract

Nuclear energy as a key low-carbon, sustainable, and clean energy source, it's proportion in the global energy structure continues to increase. However, the rapid development of nuclear energy inevitably leads to the generation of a large amount of uranium-containing wastewater, posing serious risks to environment and health. Uranium in aqueous systems predominantly exists in the form of mobile and toxic U(VI) ($UO_2^{2+}$), while U(IV) has very low solubility in water and is easier to remove. Photocatalytic reduction of highly soluble U(VI) to sparingly soluble U(IV) offers a promising route for uranium recovery. However, conventional photocatalysts with typically powder material that suffer from low activity, aggregation, and poor recyclability. Therefore, we developed a $TiO_2$ fiber membranes with a high aspect ratio, self-supporting, and non-agglomerating, demonstrating excellent performance in photocatalytic reduction of U(VI). The experimental results indicated that 400°C was the optimal heat treatment temperature, and the $TiO_2$ fiber membranes heat-treated at this temperature exhibited the highest photocatalytic reduction efficiency. At pH 5, the membranes achieved 99.0% uranium removal within 180 minutes without sacrificial agents, which 2.47 times higher than commercial Anatase $TiO_2$ powder. Moreover, the $TiO_2$ membranes still demonstrates a high removal efficiency for U(VI) after five reacting cycles. In photoluminescence spectroscopy, the emission intensity of $TiO_2$ fiber films was significantly reduced compared to that of Anatase $TiO_2$ powder, indicating effective suppression of the recombination of photogenerated electron-hole pairs. This was attributed to its one-dimensional structure, which provides a continuous path for charge transport, thereby minimizing charge recombination and enhancing reaction efficiency.


## 1. Introduction

As global energy systems shift towards low-carbon alternatives, nuclear power has emerged as a crucial option for ensuring energy security and sustainable development, owing to its high energy density and low carbon emissions[1–4]. However, the entire nuclear fuel cycle from uranium mining, fuel fabrication, reactor operation to spent fuel reprocessing generates substantial amounts of uranium containing wastewater[5, 6]. Uranium poses persistent environmental risks due to both its radioactivity and significant chemical toxicity, threatening aquatic ecosystems and human health[7–10]. This challenge is further underscored by increasingly stringent regulatory frameworks. Concurrently, the World Health Organization stipulates a maximum permissible concentration of 30 μg $L^{-1}$ for U(VI) in drinking water[11]. Consequently, developing efficient and environmentally friendly technologies for the immobilization and separation of U(VI) is of paramount importance[12].

Various conventional methods have been employed for uranium removal from aqueous environments, including precipitation[7, 13], solvent extraction[14, 15], adsorption[9, 10, 16, 17], ion exchange[18, 19] and electrocatalysis[20–22]. While these techniques offer certain advantages in specific contexts, they are generally limited by the inherent drawbacks of the technology. Precipitation generates large volumes of radioactive sludge and performs poorly at low uranium concentrations. Solvent extraction relies on toxic and volatile organic reagents, leading to secondary pollution and high operational complexity. Adsorption materials often suffer from poor selectivity and stability in real water matrices due to interference from common coexisting ions. Ion exchange resins are prone to fouling and require energy with intensive regeneration processes that produce high salinity waste streams. Electrocatalytic reduction, although effective in promoting U(VI) reduction, is heavily dependent on external power, incurs high electrode costs, and exhibits performance variability with water conductivity.

In contrast, photocatalytic reduction offers a sustainable, low-energy, and environmentally alternative. Uranium exists in natural environment two dominant oxidation states, U(IV) and U(VI). In uranium-containing wastewater, U(IV) is mainly present in the form of uranyl ions ($UO_2^{2+}$) in high environmental mobility. In contrast, U(IV) generally exists as uranium dioxide ($UO_2$), which is slightly soluble in water and thus easier separable from aqueous. By utilizing light-driven carriers generated in semiconductor materials, the reduction of soluble U(VI) to insoluble U(IV) species offers a promising strategy for immobilizing uranium from wastewater[23, 24].This approach eliminates the need for chemical reductants or external electrical input, thereby minimizing secondary waste generation while improving operational simplicity and scalability.

$TiO_2$ photocatalysts have garnered significant attention due to their high chemical stability and low cost. Since Amadelli et al. first utilized $TiO_2$ as a photocatalytic material and successfully demonstrated the photocatalytic reduction of U(VI) in 1991[25], the number of reports on U(VI) photocatalytic reduction catalysts has steadily increased [26, 27].Traditional $TiO_2$ powder suffer from several practical limitations. Particles readily agglomerate, which reduces the accessible surface area and consequently the catalytic activity. Moreover, photogenerated electrons and holes recombine at a high rate, limiting the number of charge carriers that can drive redox reactions. $TiO_2$ powder optical response is predominantly ultraviolet, so visible-light utilization is poor. Finally, the powder is difficult to recover and recycle, unfavorable to environmental sustainability.

By loading $TiO_2$ onto the substrate, its agglomeration problem can be solved, thereby improving the utilization, recovery, and recycling performance of the photocatalyst. While numerous studies have focused on immobilizing photocatalysts onto polymer matrices to improve recyclability, the inherent poor conductivity of organic materials often leads to a substantial reduction in electron transfer efficiency[28]. Furthermore, during photocatalytic reactions, the valence band of photocatalytic materials is prone to hole accumulation, a phenomenon that further impedes the transition of photogenerated electrons[29]. To mitigate hole accumulation and suppress charge carrier recombination, researchers commonly introduce sacrificial agents like methanol into the reaction system. However, this approach inevitably narrows the application scope of photocatalytic materials and incurs unnecessary resource consumption, compromising the economic viability and environmental friendliness of photocatalysis[30].

By fiberizing the photocatalyst, we can prepare a fiber membranes, which can effectively solve the aforementioned problems. The resulting fibrous network offers a large specific surface area and abundant accessible active sites, which are critical for enhancing light harvesting and interfacial charge transfer. The one-dimensional nanostructure facilitates rapid charge carrier transport along the fiber axis, reducing recombination losses and promoting photogenerated electron-hole separation. The flexibility and mechanical strength of $TiO_2$ fiber membranes facilitate the easy recovery and reuse of catalysts from the reaction system that the key advantages for practical deployment. The successful fabrication of $TiO_2$ fiber membranes hinges on precise control over material architecture and morphology. Electrospinning has proven to be a highly effective technique for producing continuous, high aspect ratio $TiO_2$ nanofibers with uniform diameter distribution and tunable porosity[31].

In this study, $TiO_2$ fiber membranes were synthesized via the electrospinning technique and employed for the efficient photocatalytic reduction of U(VI). The one-dimensional fibrous structure promotes rapid migration of photogenerated carriers and effectively suppresses charge-carrier recombination. Its large specific surface area enhances the accessibility of active sites, thereby boosting photocatalytic performance. By systematically comparing the effects of various calcination temperatures on the material's structure, morphology, mechanical strength, and photo-electrochemical properties, the $TiO_2$ fibrous membrane calcined at 400°C was identified as exhibiting the highest photocatalytic efficiency. Notably, the photocatalytic system reduces U(VI) to U(IV) directly via electron transfer, achieving an impressive 99.0% conversion within 180 min without the addition of any sacrificial agent. Moreover, the macroscopic fiber structure enabled convenient recovery and reuse of the catalyst. Optical and photoelectrochemical analysis revealed that, compared to Anatase $TiO_2$ powder, the bandgap of $TiO_2$ fiber membranes was reduced by 1.14 eV, and the light absorption range was extended by 14 nm, indicating a reduction in the reaction activation energy barrier, an increase in the light absorption range that enhance the efficiency of photocatalytic reduction of U(VI). These findings provide a novel and sustainable photocatalytic material for the green treatment of uranium wastewater, contributing to the advancement of nuclear environmental management.

## 2. Experimental section

# 2.1 Materials

Titanium isopropoxide (TTIP, $C_{12}H_{28}O_4Ti$, 95%) was purchased from McLean Biochemical Technology Co.Ltd(Shanghai, China). Polyvinylpyrrolidone (PVP, $(C_6H_9NO)n$, average molecular weight of 1,300,000) was procured from Shandong Keyuan Biochemical Co., Ltd. (Shandong, China). Uranyl nitrate hexahydrate ($UO_2(NO_3)_2$, ≥ 99%) was purchased from Shanghai Yien Chemical Technology Co., Ltd. (Shanghai, China). Reagents including glacial acetic acid ($CH_3COOH$, 99.5%), formic acid (HCOOH, ≥ 99%), anhydrous ethanol ($CH_3CH_2OH$, 99.7%), sodium hydroxide (NaOH, ≥ 99.9%), and sulfuric acid ($H_2SO_4$, ≥ 98%) were obtained from Chengdu Kelong Chemical Co., Ltd. (Chengdu, China).

# 2.2 Synthesis of $TiO_2$ fiber membranes

A solution was prepared by dissolving 0.60 g of polyvinylpyrrolidone in 6.20 g of ethanol, and then heated and stirred at 40°C until complete dissolution. Subsequently, 5.40 g of glacial acetic acid was added, followed by 4.40 g of titanium isopropoxide. The mixture was stirred uniformly to form a yellow, transparent spinning solution. The spinning solution was transferred into a syringe equipped with a stainless-steel needle for electrospinning to prepare $TiO_2$ precursor fiber membranes. The electrospinning parameters were set as follows: flow rate of 1.5 $mL \cdot h^{-1}$, applied voltage of 14 kV, and a needle-to-collector distance of approximately 15 cm. The process was conducted under controlled ambient conditions of 20–30°C and 40%-55% relative humidity. The $TiO_2$ precursor fiber membranes were collected and then subjected to thermal treatment in a muffle furnace. The heating rate was set at 2°C$\cdot min^{-1}$, and the membranes was held at the target temperature for 60 minutes before being naturally cooled to room temperature to obtain the desired $TiO_2$ fiber membranes.

# 2.3 Photocatalytic reduction of U(VI) experiments

The photocatalytic experiments were carried out in a 100 mL jacketed quartz cell equipped with a circulating water bath maintained at 25 ± 1°C. Aqueous U(VI) solutions of varying concentrations were added to the cell, either with 2 mL of formic acid or without any additive. The pH of the solution was adjusted to the desired level using either 10 mol·$L^{-1}$ NaOH or 1 mol·$L^{-1}$ $H_2SO_4$. Subsequently, 40 mg of the synthesized $TiO_2$ fiber membranes was added to the solution. The reaction mixture was then irradiated for 2 hours under an air atmosphere using a 300 W continuous-wave xenon lamp (Beijing Zhongjiao Jinyuan Technology Co., Ltd., Beijing, China) with a wavelength cutoff filter (λ > 420 nm). During the irradiation, 1 mL of the reaction solution was withdrawn at regular intervals. The withdrawn samples were filtered through a 0.22 μm PES syringe filter to remove the photocatalyst and obtain clear solutions for analysis. After the photocatalytic reaction, the residual uranium concentration in the sample solution was determined using an inductively coupled plasma-emission spectrometer (ICP-OES, ICAP 7400).

## 2.4 Material characterization

Phase analysis was performed using X-ray diffraction (XRD) on a PANalytical Empyrean diffractometer (PANalytical, Almelo, Netherlands) operating at 40 kV and 40 mA with Cu Kα radiation (λ = 1.5418 Å). The microstructure of the materials were examined using a Hitachi SU8100 scanning electron microscope (SEM). Elemental composition analyses were conducted using a Kratos AXIS Ultra DLD X-ray photoelectron spectrometer (XPS) with an Al Kα X-ray source. Binding energies (BE) were calibrated using the C 1s peak at 284.8 eV. Optical and optoelectronic properties were investigated using a Shimadzu UV-2802 UV-Vis spectrophotometer (Shimadzu, Kyoto, Japan) equipped with an integrating sphere, using barium sulfate ($BaSO_4$) as a reflectance standard, over a wavelength range of 200–800 nm. Electrochemical measurements were performed using a CHI 660E electrochemical workstation (Shanghai Chenhua, Shanghai, China) with a three-electrode system. The system consisted of the $TiO_2$ fiber membranes as the working electrode, a saturated Ag/AgCl electrode as the reference electrode, and a platinum (Pt) electrode as the counter electrode, under simulated solar irradiation from a 300 W xenon lamp. The chemical structure of the materials was analyzed using Fourier transform infrared (FT-IR) spectroscopy with a PerkinElmer ThermoNicolet Smart-380 instrument, scanning from 4000 to 400 $cm^{-1}$. Thermal stability was investigated by simultaneous thermogravimetric and differential scanning calorimetry (TGA-DSC) using a TGA/DSC instrument. Samples were heated from 25°C to 1000°C at a rate of 5°C·$min^{-1}$ under an air atmosphere. The Brunauer-Emmett-Teller (BET) surface areas of the ffbers were tested using speciffc surface area instrument (JW-BK112,JWGB Sci & Tech).

## 3. Results and discussion

## 3.1. Structure characterization

Figure 1(a) shown the FT-IR spectra of $TiO_2$ fiber membranes heat-treated at different temperatures. The broad and strong absorption band at 2900–3600 $cm^{-1}$ in the precursor fiber corresponds to O-H stretching vibrations, attributed to adsorbed water molecules and hydroxyl groups from ethanol, acetic acid, and the hydrolysis of titanium isopropoxide. As the temperature increases, the intensity of this band decreases significantly, indicating the desorption of water and the condensation of hydroxyl groups. The peak at 1650 $cm^{-1}$ was assigned to C = O stretching from acetic acid. The peaks at 1541 $cm^{-1}$ and 1438 $cm^{-1}$ are respectively attributed to the asymmetric and symmetric stretching vibrations of carboxylate (-$COO^-$), confirming the coordination between carboxylate groups and Ti ions[32, 33]. The separation (Δv) between these two peaks was 103 $cm^{-1}$, which suggested a chelating bidentate coordination mode of carboxylate to Ti[34, 35]. The absorption at 442 $cm^{-1}$ corresponded to Ti-O-Ti stretching, indicating the onset of crystallization into the Anatase phase at 400°C.

Table 1
The major FT-IR absorption bands and assignments.

| Assignment | v(O-H) | v(C = O) | $v^{as}(COO^-)$ | $v^{s}(COO^-)$ | v(Ti-O-Ti) |
|---|---|---|---|---|---|
| Band ($cm^{-1}$) | 3412 | 1650 | 1541 | 1438 | 442 |

As shown in Fig. 1(b), the thermal decomposition of the precursor fibers in air proceeded in three stages. The first stage below 150°C shown a mass loss of about 15.69% in the TG curve, due to the evaporation of solvents such as ethanol and water. This was consistent with the reduced intensity of the FT-IR absorption band at 2900–3600 $cm^{-1}$ after heating at 150°C. The second stage between 150°C and 400°C exhibited a mass loss of about 24.31% and a distinct exothermic peak appeared at 339°C in the DSC curve, corresponding to the further decomposition of organic components and the crystallization of $TiO_2$. Accordingly, the organic peaks at FT-IR spectra gradually disappear by 300°C, and the Ti-O-Ti vibration emerges at 400°C. Above 400°C, a further mass loss of about 13.09% and multiple exothermic peaks are observed, associated with residual organic decomposition and continued crystallization.

The XRD patterns in Fig. 1(c) revealed the phase evolution of the material. No distinct diffraction peaks were observed at 300°C, indicating that the fiber membrane was an amorphous structure at this temperature. At 400°C, diffraction peaks the fiber membrane appeared at 25.3°, 37.8°, 48.0°, 53.9°, and 55.1°, indexed to the (101), (004), (200), (105), and (211) planes of Anatase $TiO_2$ (PDF#75-1537), confirming crystallization into the Anatase phase. This aligns with the appearance of the Ti-O-Ti vibration in the FT-IR spectrum at 400 ℃. With increasing temperature from 400°C to 600°C, the Anatase peaks intensify, indicating that $TiO_2$ fiber membrane was improved crystallinity. At 700°C, new peaks emerged at 27.5°, 36.1°, 41.3°, 44.1°, 54.4°, and 56.7°, corresponding to the (110), (101), (111), (210), (211), and (220) planes of the Rutile phase (PDF#87–0710), demonstrating a partial phase transformation from Anatase to Rutile in the $TiO_2$ fiber membrane. The BET surface area and pore volume of $TiO_2$ fiber membranes (Fig. 1d and 1e) decreased continuously from 400°C to 600°C, which were related to crystal growth, particle agglomeration, and densification of the fibers. The sample treated at 400°C possesses the highest specific surface area and pore volume. SEM images (Fig. 1f–1h) illustrated the morphological evolution. At 400°C, the fibers exhibited a rough surface and uniformly distributed pores, resulting from the incomplete decomposition of organics and the release of gaseous products. This porous structure favors high surface area and efficient mass transport. At 500°C, the fibers became smoother with reduced porosity due to further organic removal and crystal growth. At 600°C, the fibers appeared denser with a smoother surface and significantly diminished porosity, indicating advanced sintering and densification. EDS mapping of the sample treated at 400°C (Fig. 1f1–f3) shown a homogeneous distribution of Ti and O, along with detectable C signals from residual organic carbon. Combined with the XRD results, which confirmed the formation of a uniform Anatase phase at this temperature.

In summary, the thermal treatment temperature critically influenced the chemical composition, crystal structure, porosity, and morphology of the $TiO_2$ nanofibers. The sample treated at 400°C exhibited an Anatase phase, a porous fibrous structure, and the highest specific surface area, which were favorable properties for photocatalytic applications.

## 3.2 Optical and electrochemical properties

The light absorption capability is a fundamental property of semiconductor materials. As shown in Fig. 2(a), the UV-Vis absorption spectra of $TiO_2$ fiber membranes calcined at different temperatures revealed distinct absorption edges. The sample treated at 400°C exhibited an absorption edge at approximately 398 nm with its light absorption range expanded by 10 nm compared to Anatase $TiO_2$ powder[36]. As the calcination temperature increases to 500°C and 600°C, a slight blue shift of the absorption edge was observed, reaching 392 nm for the 600°C sample. As the heat treatment temperature of $TiO_2$ fiber membranes increased, the light absorption range of the photocatalyst gradually decreased. However, a slight red shift back to 393 nm occured for the sample calcined at 700°C. This reversal was attributed to a phase transformation from pure Anatase to a mixed Anatase/Rutile phase, which altered the band structure. We can clearly observe that $TiO_2$ fiber membranes heat treatment at 400°C and 500°C exhibited broader visible light absorption in the UV-Vis spectra, with ranges of 390–600 nm and 390–500 nm, respectively. In contrast, $TiO_2$ fiber membranes heat treatment at 600°C and 700°C did not display similar behavior.The corresponding optical band gaps (Eg) were determined using the Tauc plot method (Fig. 2b). Consistent with the absorption edge shift, the band gap of $TiO_2$ fiber films increased from 3.31 eV for the 400°C sample to 3.34 eV for the 600°C sample, which was about 0.05 eV less than that of Anatase $TiO_2$ powder[36]. The blue shift and associated band gap widening imply a higher activation energy barrier for photo-induced redox reactions. Conversely, the sample treated at 700°C shown a reduced band gap of 3.33 eV, again due to the phase change of $TiO_2$. Overall, the 400°C sample possessed the narrowest band gap and the best light-harvesting ability among the samples.

The efficiency of charge carrier separation and transport critically influences photocatalytic performance. Electrochemical impedance spectroscopy (EIS) was employed to evaluate the charge transfer resistance, as presented in the Nyquist plots (Fig. 2c). A smaller arc radius corresponded to lower charge transfer resistance. The 400°C sample exhibited the smallest semicircle, indicating the most efficient charge separation and transport which minimized the recombination of photogenerated electron-hole pairs and promoted their rapid migration to the surface for redox reactions. The flat-band potentials (Efb) of the samples were estimated from Mott-Schottky (M-S) plots measured at frequencies of 800, 900, and 1000 kHz (Fig. 2d). The positive slopes of all M-S curves confirmed the n-type semiconductor nature of the $TiO_2$ fibers membranes. The Efb values became more positive with increasing calcination temperature, shifting from − 0.26 V for the 400°C sample to -0.17 V (vs. Ag/AgCl) for the 700°C sample. Combining the optical band gap (Eg) from Tauc plots and the flat-band potential (Efb) from M-S analysis, the energy band structures were constructed (Fig. 2e). For n-type semiconductors, the conduction band minimum (CBM) is approximately equal to Efb. Consequently, the CBM positions were determined as -0.26, -0.21, -0.18, and − 0.17 eV (vs. Ag/AgCl) for $TiO_2$ fiber membranes treated at 400, 500, 600, and 700°C, respectively. A more negative CBM signifies stronger reducing power of photogenerated electrons, which $TiO_2$ fiber membranes heat-treated at 400 ℃ exhibited a lower conduction band value, indicating that its photogenerated electrons possess stronger reducing capability. The valence band maximum (VBM) positions, calculated using the formula $E_{VBM} = E_{CBM} + E_g$, were 3.05, 3.13, 3.16, and 3.16 eV (vs. Ag/AgCl), respectively. Figure 2 (f) displayed the photoluminescence (PL) spectra of Anatase $TiO_2$ powder and $TiO_2$ fiber membranes heat-treated at 400 ℃-700 ℃, all excited with a 300 nm wavelength. The intrinsic emission peak appeared at about 362 nm. Compared with the powder, the fiber membranes shown a markedly lower PL intensity, and this

intensity diminished progressively as the sintering temperature rises. The membranes sintered at 400°C exhibited the weakest PL, indicating that recombination of photogenerated electron–hole pairs was most effectively suppressed at this temperature[37].

In summary, the 400°C $TiO_2$ fiber membranes displayed the most favorable electronic characteristics for photocatalysis. The 400°C $TiO_2$ fiber membranes had the widest range of light absorption, thereby achieving maximum light absorption efficiency and had the most negative conduction band minimum, indicating the strongest reducing power of photogenerated electrons. The sample also exhibited the lowest charge transfer resistance, reflecting highly efficient carrier transport. Its photoluminescence intensity was the weakest among these $TiO_2$ fiber membranes, suggesting a pronounced suppression of electron–hole recombination. Collectively, these attributed produce a synergistic effect that was expected to translate into superior photocatalytic performance.

## 3.3. Photocatalytic reduction of uranium performances

Table 2
The different catalysts for U(VI) photoreduction in literatures.

| Catalyst | Conditions | Sacrifice | Removal ratio | Ref. |
|---|---|---|---|---|
| $TiO_2$ fiber membranes | $C_0$=20ppm, m/V = 0.5g/L, pH = 5 | None | 99.0% in 180 min | This work |
| $Ti_{1-x}O_2$ | $C_0$=8ppm, m/V = 0.25g/L, pH = 7 | None | 38.5% in 120 min | [27] |
| pristine $TiO_2$ fiber membranes | $C_0$=50ppm, m/V = 0.2g/L, pH = 6 | None | 8.6% in 120 min | [36] |
| P-g-$C_3N_4$ | $C_0$=30ppm, m/V = 0.5g/L, pH = 7 | 2.5% Methanol | 90% in 20 min | [38] |
| ZnO/rectorite | $C_0$=5ppm, m/V = 1.5 g/L, pH = 5 | 1.0 mol/L Methanol | 99% in 240 min | [39] |

Figure 3(a) presented the photocatalytic U(VI) reduction efficiency of $TiO_2$ fiber membranes treated at different temperatures was evaluated under UV light. The membranes treated at 400°C exhibited the highest photocatalytic activity. With increasing treatment temperature, the photocatalytic efficiency decreased, attributed to the increased in heat treatment temperature, which leaded to the growth of $TiO_2$ grain size and subsequent phase transformation. The structural changed affecte the light absorption and photoelectrical properties, resulting in an increase in charge transfer resistance, a decrease in electron reduction ability, and an increase in the recombination rate of photogenerated carriers. These factors had a negative impact on the catalytic performance. Notably, the 400°C membranes achieved a U(VI) removal rate of 99.9% within 120 minutes. This superior performance was primarily due to its advantageous structural characteristics at 400°C. The fiber membranes heat-treated at 400°C Celsius possessed a porous structure with uniform pores and a large specific surface area, which provided abundant active sites for the photocatalytic reaction, significantly enhancing the contact between U(VI) and the catalyst surface. To further assessed the photocatalytic capability of the 400°C treated membranes and determined optimal operating conditions, subsequent experiments were conducted.

Figure 3(b) presented the photocatalytic reduction of U(VI) by the 400°C treated membranes was investigated under various pH conditions. The results shown that, at pH values of 0 and 1, the $TiO_2$ fiber membranes exhibited no photocatalytic activity for U(VI) reduction. This was attributed to the high concentration of $H^+$ ions in strongly acidic aqueous solutions, which competed with U(VI) ions for photogenerated electrons. This competition significantly reduces the efficiency of photocatalytic reduction. As the pH increased, the photocatalytic reduction efficiency of U(VI) gradually enhanced. At pH = 5, a U(VI) removal rate of 99.9% was achieved within 120 minutes. Figure 3(c) presented the effect of different U(VI) concentrations on the photocatalytic reduction by the 400°C treated membranes was examined. For U(VI) concentrations below 20 mg $L^{-1}$, removal rates of 99.9% were observed within 120 minutes. However, as the substrate concentration increased, the photocatalytic efficiency of the $TiO_2$ nanofiber membranes decreased. This was likely because at excessively high U(VI) concentrations, the adsorption of U(VI) on the $TiO_2$ surface becomes supersaturated, and the excess U(VI) occupied a significant number of active sites.

Figure 3(d) presented the influence of formic acid (HCOOH) as a sacrificial agent on the photocatalytic reduction of U(VI) was investigated. Formic acid, an excellent hole scavenger, rapidly consumes photogenerated holes, promoting the separation of electron-hole pairs and enabling more photogenerated electrons to participate in the U(VI) reduction reaction, thereby enhancing photocatalytic activity. Under formic acid was added at a volume ratio of 4% conditions, the removal efficiency of U(VI) from a 20 mg·$L^{-1}$ solution reached 99.9% within 120 minutes. In the absence of formic acid, the U(VI) removal efficiency reached 95.7% within 120 minutes and 99.0% after 180 minutes

which 2.47 times higher than commercial Anatase $TiO_2$ powder[36]. This indicated that the $TiO_2$ fiber membranes exhibited a high photocatalytic reduction rate for U(VI) even without the addition of formic acid.

Figure 3(e) presented the influence of common interfering metal ions on the photocatalytic reduction of U(VI). The presence of 100ppm $Sr^{2+}$, $K^+$, and $Na^+$ exhibited a slight inhibitory effect on U(VI) removal, likely attributed to competition for active sites on the $TiO_2$ composite fiber membranes. Nevertheless, even under these competitive conditions, the membranes achieved a U(VI) removal efficiency exceeding 97% within 2 hours of irradiation. This underscores the material's robust and stable uranium extraction capability in complex aqueous matrices. Figure 3(f) illustrates the effect of inorganic anions. The addition of 100ppm $Cl^-$, $NO_3^-$, and $SO_4^{2-}$ had a negligible impact on the photocatalytic reduction of U(VI). This observation highlights the excellent resistance of the $TiO_2$ composite fiber membranes to anionic interference, suggesting its potential for selective and efficient U(VI) removal in real water bodies.

Figure 3(g) presented the role of different scavengers in the photocatalytic reduction of U(VI) was investigated. $Ag^+$ as a potent electron scavenger, resulted in a high concentration of residual U(VI) after 120 minutes of illumination, as the captured electrons severely limited the reduction reaction. This visually confirmed that photogenerated electrons were the decisive active species driving the reduction of U(VI) to U(IV). In contrast, HCOOH as a hole scavenger, lead to an enhanced U(VI) reduction efficiency. This was attributed to the suppression of electron-hole recombination by hole scavenging, prolonging the electron lifetime and allowing more electrons to participate in U(VI) reduction. $C_3H_8O$ role as a hydroxyl radical scavenger, exhibited the fastest curve decline, suggesting that hydroxyl radicals might negatively impact the reduction process by competitively consuming photogenerated electrons or oxidizing the generated U(IV) species. By quenching ·OH, photogenerated electrons were more selectively and efficiently utilized for U(VI) reduction, significantly accelerating the reaction rate. Collectively, these scavenger studies unequivocally demonstrated that photogenerated electrons were the dominant active species for U(VI) reduction. The mechanism of photocatalytic reduction of U(VI) by $TiO_2$ fiber membranes was the direct reduction of U(VI) by these electrons, while the scavenger just promotes this process.

Fig. (h) exhibited the recyclability of the $TiO_2$ composite fiber membranes was assessed over five cycles of U(VI) removal. Recyclability is a crucial metric for evaluating the practical application potential of photocatalysts. The material maintained exceptionally high catalytic activity during the first two cycles, comparable to the initial activity with removal rates of 98.9% and 98.2%, respectively, which reflected good structural stability. A noticeable decline in the removal rate was observed starting from the third cycle. After the fifth cycle, the removal rate was 80.8%. This reduction may be attributed to slight loss of active components or structural damage on the fiber membrane surface caused by fluid flushing during repeated cycling. These results indicated that the $TiO_2$ composite fiber membranes possesses good practical application potential, offering a viable technological solution for the continuous treatment of uranium-containing wastewater. As shown in Fig. (i) there was no significant change in the concentration of titanium ions during the photocatalytic process, indicating the good stability of the photocatalytic material.

## 3.4 Analysis of reduction products

X-ray photoelectron spectroscopy (XPS) was employed to characterize the $TiO_2$ nanofiber membranes, investigating the elemental changes on the membranes surface before and after photocatalysis. The survey XPS spectrum of the pristine $TiO_2$ nanofiber membranes (Fig. 4a) clearly shown prominent peaks corresponding to O 1s, Ti 2p, and C 1s. This confirmed that the primary elemental constituents of the fiber membranes were Ti and O, with a minor presence of C, and no other impurity elements were detected. Following photocatalytic reduction, the XPS survey spectrum still exhibited the original Ti 2p, O 1s, and C 1s peaks without significant shifts. This further validated the structural stability of the $TiO_2$ nanofiber membranes as a photocatalyst. Importantly, the post-photocatalysis survey spectrum revealed the appearance of U 4f characteristic peaks. As shown in Fig. 4(c), distinct peaks for U 4f 5/2 and U 4f 7/2were observed at binding energies of 391.70 eV and 380.99 eV, respectively. The energy separation of 10.71 eV between these peaks is characteristic of U(IV) valence states[40]. It was suggested that aqueous U(VI) was reduced to U(IV) by the $TiO_2$ photocatalyst. Figure 4(b) presented the high-resolution O 1s XPS spectra. The peak at 529.82 eV was attributed to lattice oxygen, corresponding to the Ti-O-Ti bonds within the $TiO_2$ crystal structure. The peak at 531.38 eV was assigned to surface hydroxyl oxygen, which originates from adsorbed water or surface hydroxyl groups. The presence of hydroxyl oxygen reflected the surface hydrophilicity and potential active sites. Deconvolution of the O 1s spectrum allowed for the quantitative analysis of the relative areas of these oxygen species. The peak area of hydroxyl groups increased after photocatalysis compared to before photocatalysis. This enhancement was attributed to the photocatalytic reaction, where the generation of hydroxyl radicals (·OH) from water ($H_2O + h^+ \rightarrow \cdot OH + H^+$) leaded to an increased proportion of surface hydroxyl oxygen[41, 42].

Figure 4(d) displayed the X-ray diffraction (XRD) patterns of the $TiO_2$ fiber membranes, before and after the photocatalytic reduction of U(VI). The standard card PDF#75-1537 for Anatase $TiO_2$ was used as a reference for phase identification. The XRD results demonstrated that the $TiO_2$ fiber membranes maintained its pure Anatase phase even after the photocatalytic reaction. However, no new characteristic peaks of

the product appeared, which may be due to the formation of amorphous U(IV) precipitate. $TiO_2$ fiber membranes structural stability was crucial and provided a strong foundation for the potential cyclic reusability of the material.

## 4. Conclusion

In this study, flexible $TiO_2$ fiber membranes were successfully fabricated via electrospinning and demonstrated exceptional performance in the photocatalytic reduction of U(VI) without the need for sacrificial agents. The U(VI) removal efficiency of 99.0% was achieved within 180 minutes with 2.47 times higher than that of conventional Anatase $TiO_2$ powder that attributed to enhanced light absorption and improved charge carrier dynamics. The light absorption range was extended by 10 nm, improving the utilization efficiency of light and thereby enhancing the efficiency of the photocatalytic reduction reaction of U(VI). The extremely low conduction band position at -0.26 eV indicated that strong reducing capability of photogenerated electrons provided sufficient driving force for the reduction of U(VI) to U(IV). The macroscopic fibrous architecture facilitated rapid transport of photogenerated carriers that compared with the $TiO_2$ powder, the fiber membranes shown a markedly lower PL intensity which effectively suppresses charge recombination and consequently enhances photocatalytic activity. Moreover, the flexible of the membranes allows for facile separation and recovery from aqueous solutions, overcoming the inherent challenges associated with powder-based catalysts. After five consecutive cycles, the membranes retained approximately 80.8% of removal efficiency, demonstrating excellent structural and catalytic stability.

Notably, the material maintained consistent performance under varying pH conditions and in the presence of common inorganic ions, indicating stability in complex aqueous environments. These findings highlight the significant potential of $TiO_2$ fiber membranes as a practical, reusable, and sustainable photocatalytic material for the green remediation of uranium contaminated water.

## Declarations

# Author Contribution

Yongshuang You: Formal analysis, Methodology, Data curation, Resources, Investigation, Writing - original draft, Writing - review & editing, Funding acquisition. Shuying Shi: Conceptualization, Methodology, Validation, Writing - review & editing.Shuangyang Zhou: Software, Validation. Xianqing Chen: Writing - review & editing. Lisha Yang: Writing - review & editing. Yanliu: Writing - review & editing. Xinke Dan: Software, Validation.Jiawei Tian: Software, Validation. Jianwen Zhang: Supervision, Project administration, Funding acquisition. Hao deng: Supervision, Project administration, Funding acquisition.

# Acknowledgments

This work was supported by the Postgraduate Innovation Fund of Southwest University of Science and Technology (No. 25ycx1021), the Natural Science Foundation of Southwest University of Science and Technology (No. 21zx7134, No. 25zx7135), the Natural Science Foundation of Sichuan Province (No. 2026NSFSC0061) and the National Natural Science Foundation of China (No. 22106127) .

## References

1. Ye Y, Jin J, Chen F, Dionysiou DD, Feng Y, Liang B, Cheng H-Y, Qin Z, Tang X, Li H, Yntema D, Li C, Chen Y, Wang Y (2022) Removal and Recovery of Aqueous U(VI) by Heterogeneous Photocatalysis: Progress and Challenges. Chem Eng J 450:138317. https://doi.org/10.1016/j.cej.2022.138317
2. Chen T, Yu K, Dong C, Yuan X, Gong X, Lian J, Cao X, Li M, Zhou L, Hu B, He R, Zhu W, Wang X (2022) Advanced Photocatalysts for Uranium Extraction: Elaborate Design and Future Perspectives. Coord Chem Rev 467:214615. https://doi.org/10.1016/j.ccr.2022.214615
3. Kumar V, Singh V, Kim K-H, Kwon EE, Younis SA (2021) Metal-Organic Frameworks for Photocatalytic Detoxification of Chromium and Uranium in Water. Coord Chem Rev 447:214148. https://doi.org/10.1016/j.ccr.2021.214148
4. Yang W, Pan Q, Song S, Zhang H (2019) Metal–Organic Framework-Based Materials for the Recovery of Uranium from Aqueous Solutions. Inorg Chem Front 6(8):1924–1937. https://doi.org/10.1039/C9QI00386J
5. Li S, Yang X, Cui Z, Xu Y, Niu Z, Li P, Pan D, Wu W (2021) Efficient Photoreduction Strategy for Uranium Immobilization Based on Graphite Carbon Nitride/Perovskite Oxide Heterojunction Nanocomposites. Appl Catal B 298:120625. https://doi.org/10.1016/j.apcatb.2021.120625

6. Abdi S, Nasiri M, Mesbahi A, Khani MH (2017) Investigation of Uranium (VI) Adsorption by Polypyrrole. J Hazard Mater 332:132–139. https://doi.org/10.1016/j.jhazmat.2017.01.013
7. *A 3,2-Hydroxypyridinone-based Decorporation Agent that Removes Uranium from Bones In Vivo | Nature Communications*. https://www.nature.com/articles/s41467-019-10276-z (accessed 2026-05-19)
8. Li Z-J, Huang Z-W, Guo W-L, Wang L, Zheng L-R, Chai Z-F, Shi W-Q (2017) Enhanced Photocatalytic Removal of Uranium(VI) from Aqueous Solution by Magnetic TiO2/Fe3O4 and Its Graphene Composite. Environ Sci Technol 51(10):5666–5674. https://doi.org/10.1021/acs.est.6b05313
9. Liang P, Yuan L, Deng H, Wang X, Wang L, Li Z, Luo S, Shi W (2020) Photocatalytic Reduction of Uranium(VI) by Magnetic ZnFe2O4 under Visible Light. Appl Catal B 267:118688. https://doi.org/10.1016/j.apcatb.2020.118688
10. Zhang P, Wang L, Yuan L-Y, Lan J-H, Chai Z-F, Shi W-Q (2019) Sorption of Eu(III) on MXene-Derived Titanate Structures: The Effect of Nano-Confined Space. Chem Eng J 370:1200–1209. https://doi.org/10.1016/j.cej.2019.03.286
11. Ma M, Wang R, Xu L, Xu M, Liu S (2020) Emerging Health Risks and Underlying Toxicological Mechanisms of Uranium Contamination: Lessons from the Past Two Decades. Environ Int 145:106107. https://doi.org/10.1016/j.envint.2020.106107
12. Liu X, Bi R-X, Zhang C-R, Luo Q-X, Liang R-P, Qiu J-D (2023) SnS2-Covalent Organic Framework Z-Scheme van Der Waals Heterojunction for Enhanced Photocatalytic Reduction of Uranium (VI) in Rare Earth Tailings Wastewater. Chem Eng J 460:141756. https://doi.org/10.1016/j.cej.2023.141756
13. Oh M, Jung JY, Jun BM, Lee K, Eun HC (2025) Evaluation of Uranium-Removal Characteristics From Soil-Washed Wastewater Using Precipitation Methods. J Nuclear Fuel Cycle Waste Technol 23(1):131–138. https://doi.org/10.7733/jnfcwt.2025.009
14. Enhanced *Photocatalytic Removal of Uranium(VI) from Aqueous Solution by Magnetic TiO2/Fe3O4 and Its Graphene Composite | Environmental Science & Technology*. https://pubs.acs.org/doi/10.1021/acs.est.6b05313?ref=PDF (accessed 2026-05-19)
15. Mo Z, Long J, Wang W, Qian X, Wang Q, Guo Z, Lei Z, Hu Y, Bayoussef A, Hu P (2025) Extraction of Uranium from Low-Concentration Solutions Using P204 Bubbling Organic Liquid Membrane Technology. Physicochem Probl Min Process. https://doi.org/10.37190/ppmp/215176
16. *Frontiers | Advanced materials for uranium adsorption: a mini review of recent developments*. https://www.frontiersin.org/journals/materials/articles/10.3389/fmats.(2025) 1541204/full (accessed 2026-05-19)
17. Zr-Gallic Acid Based Metal Organic Compound as Adsorbent for Extraction of Uranium(vi) from Nitrate Solution: Adsorption Behaviors and Mechanisms. RSC Adv (2026) *16* (4), 3057–3076. https://doi.org/10.1039/d5ra05880e
18. Chen F, Lv M, Ye Y, Miao S, Tang X, Liu Y, Liang B, Qin Z, Chen Y, He Z, Wang Y (2022) Insights on Uranium Removal by Ion Exchange Columns: The Deactivation Mechanisms, and an Overlooked Biological Pathway. Chem Eng J 434:134708. https://doi.org/10.1016/j.cej.2022.134708
19. *Open-Framework Vanadate as Efficient Ion Exchanger for Uranyl Removal | Environmental Science & Technology*. https://pubs.acs.org/doi/10.1021/acs.est.4c03703 (accessed 2026-05-19)
20. *A half-wave rectified alternating current electrochemical method for uranium extraction from seawater | Nature Energy*. https://www.nature.com/articles/nenergy20177 (accessed 2026-05-19)
21. *Uranium In Situ Electrolytic Deposition with a Reusable Functional Graphene-Foam Electrode | Request PDF*. https://www.researchgate.net/publication/353685942_Uranium_In_Situ_Electrolytic_Deposition_with_a_Reusable_Functional_Graphene-Foam_Electrode (accessed 2026-05-19)
22. *Electrocatalytic Removal of Low-Concentration Uranium Using $TiO_2$ Nanotube Arrays/Ti Mesh Electrodes*. http://ouci.dntb.gov.ua/en/works/9jq52MjI/ (accessed 2026-05-19)
23. Li Z, Zhang Z, Zhu X, Meng C, Dong Z, Xiao S, Wang Y, Wang Y, Cao X, Liu Y (2023) Exciton Dissociation and Transfer Behavior and Surface Reaction Mechanism in Donor–Acceptor Organic Semiconductor Photocatalytic Separation of Uranium. Appl Catal B 332:122751. https://doi.org/10.1016/j.apcatb.2023.122751
24. Yu K, Tang L, Cao X, Guo Z, Zhang Y, Li N, Dong C, Gong X, Chen T, He R, Zhu W (2022) Semiconducting Metal–Organic Frameworks Decorated with Spatially Separated Dual Cocatalysts for Efficient Uranium(VI) Photoreduction. Adv Funct Mater 32. https://doi.org/10.1002/adfm.202200315
25. Amadelli R, Maldotti A, Sostero S, Carassiti V (1991) Photodeposition of Uranium Oxides onto TiO2 from Aqueous Uranyl Solutions. J Chem Soc Faraday Trans 87(19):3267–3273. https://doi.org/10.1039/FT9918703267
26. Li P, Wang J, Wang Y, Liang J, He B, Pan D, Fan Q, Wang X (2019) Photoconversion of U(VI) by TiO2: An Efficient Strategy for Seawater Uranium Extraction. Chem Eng J 365:231–241. https://doi.org/10.1016/j.cej.2019.02.013

27. Gong X, Tang L, Zou J, Guo Z, Li Y, Lei J, Liu H, Liu M, Zhou L, Huang P, Ruan H, Lu Y, Zhu W, He R (2022) Introduction of Cation Vacancies and Iron Doping into TiO2 Enabling Efficient Uranium Photoreduction. J Hazard Mater 423:126935. https://doi.org/10.1016/j.jhazmat.2021.126935
28. Li W, Liao G, Duan W, Gao F, Wang Y, Cui R, Wang X, Wang C (2024) Synergistically Electronic Interacted PVDF/CdS/TiO2 Organic-Inorganic Photocatalytic Membrane for Multi-Field Driven Panel Wastewater Purification. Appl Catal B: Environ Energy 354:124108. https://doi.org/10.1016/j.apcatb.2024.124108
29. Wang P, Benitez G, Houle FA (2025) Influence of Hole Transport and Thermal Reactions in Photo-Driven Water Oxidation Kinetics on Crystalline TiO2. ACS Catal 15(9):7653–7665. https://doi.org/10.1021/acscatal.5c00945
30. Zhang T, Lu S (2022) Sacrificial Agents for Photocatalytic Hydrogen Production: Effects, Cost, and Development. Chem Catal 2(7):1502–1505. https://doi.org/10.1016/j.checat.2022.06.023
31. *Biomimetic design of highly flexible metal oxide nanofibrous membranes with exceptional mechanical performance for superior phosphopeptide enrichment | Nano Research | Springer Nature Link*. https://link.springer.com/article/10.1007/s12274-023-6277-7 (accessed 2026-05-19)
32. Tsai MT (2002) Effects of Hydrolysis Processing on the Character of Forsterite Gel Fibers. Part II: Crystallites and Microstructural Evolutions. J Eur Ceram Soc 22(7):1085–1094
33. Two novel polytitanium precursors containing linear Ti–(OH)2–Ti chains applied for the preparation of titanium dioxide fibers | Applied Physics A |. Springer Nat Link. https://link.springer.com/article/10.1007/s00339-015-9468-6 (accessed 2026-05-19).
34. Deacon GB, Phillips RJ (1980) Relationships between the Carbon-Oxygen Stretching Frequencies of Carboxylato Complexes and the Type of Carboxylate Coordination. Coord Chem Rev 33(3):227–250. https://doi.org/10.1016/S0010-8545(00)80455-5
35. *(PDF) Infrared and Raman Spectra of Inorganic and Coordination Compounds*. https://www.academia.edu/39769772/Infrared_and_Raman_Spectra_of_Inorganic_and_Coordination_Compounds (accessed 2026-05-19)
36. Cai Z, Wang J, Fu H, Pan Y, Ma M, Zhong Y, Deng Y, Wei Y, Fujita T, Wang X (2024) Designing Flexible TiO2/SrTiO3/BiOBr Recyclable Fiber Membrane with Spatial Dual Oxidation Sites for Photocatalytic Uranium Extraction under Visible Light. Chem Eng J 500:156785. https://doi.org/10.1016/j.cej.2024.156785
37. Harvesting *the Vibration Energy of CdS for High-Efficient Piezo-Photocatalysis Removal of U(VI): Roles of Shape Dependent and Piezoelectric Polarization - Dong – 2024 - ENERGY & ENVIRONMENTAL MATERIALS - Wiley Online Library*. https://onlinelibrary.wiley.com/doi/full/10.1002/eem2.12705 (accessed 2026-05-19)
38. Wu X, Jiang S, Song S, Sun C (2018) Constructing Effective Photocatalytic Purification System with P-Introduced g-C3N4 for Elimination of UO22+. Appl Surf Sci 430:371–379. https://doi.org/10.1016/j.apsusc.2017.06.065
39. Guo Y, Li L, Li Y, Li Z, Wang X, Wang G (2016) Adsorption and Photocatalytic Reduction Activity of Uranium(VI) on Zinc Oxide/Rectorite Composite Enhanced with Methanol as Sacrificial Organics. J Radioanal Nucl Chem 310(2):883–890. https://doi.org/10.1007/s10967-016-4820-7
40. *Direct observation of pure pentavalent uranium in U2O5 thin films by high resolution photoemission spectroscopy | Scientific Reports*. https://www.nature.com/articles/s41598-018-26594-z (accessed 2026-05-19)
41. *Characterization of photocatalytic TiO2 powder under varied environments using near ambient pressure X-ray photoelectron spectroscopy | Scientific Reports*. https://www.nature.com/articles/srep43298 (accessed 2026-05-19)
42. *Ti3 + Self-Doping of TiO2 Boosts Its Photocatalytic Performance: A Synergistic Mechanism*. https://www.mdpi.com/1420-3049/29/22/5385 (accessed 2026-05-19)

## Figures

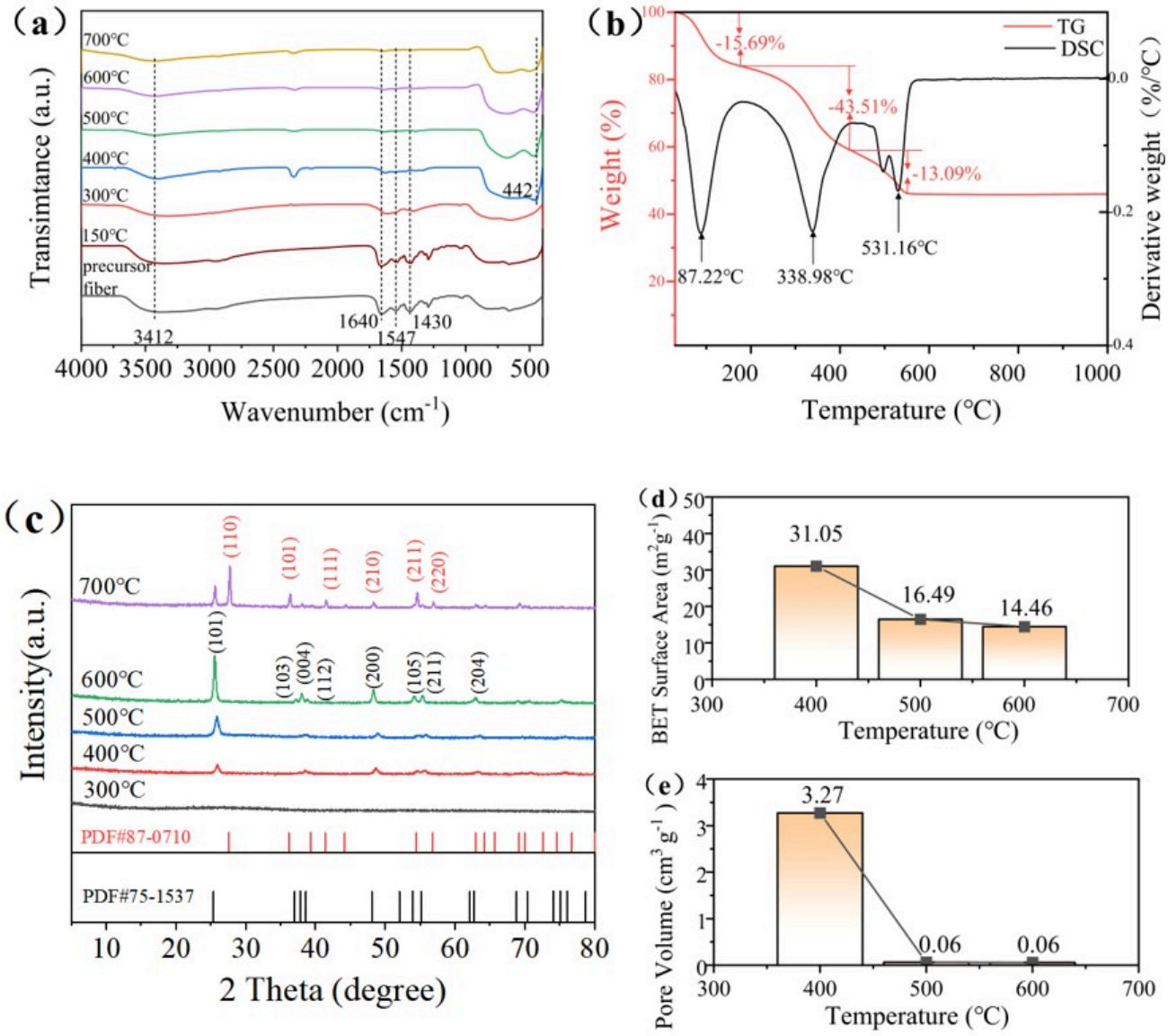



**Figure 1**

(a) FT-IR spectra of $TiO_2$ fiber membranes. (b) TGA and DSC of the $TiO_2$ precursor fiber membranes under an air atmosphere. (c) XRD patterns of $TiO_2$ fiber membranes. (d) & (e) Specific surface area and pore volume of $TiO_2$ fiber membranes. (f)-(h) SEM images at 400°C, 500°C, and 600°C of $TiO_2$ fiber membranes respectively. (f 1)-(f 3) EDS spectra at 400°C of $TiO_2$ fiber membranes.

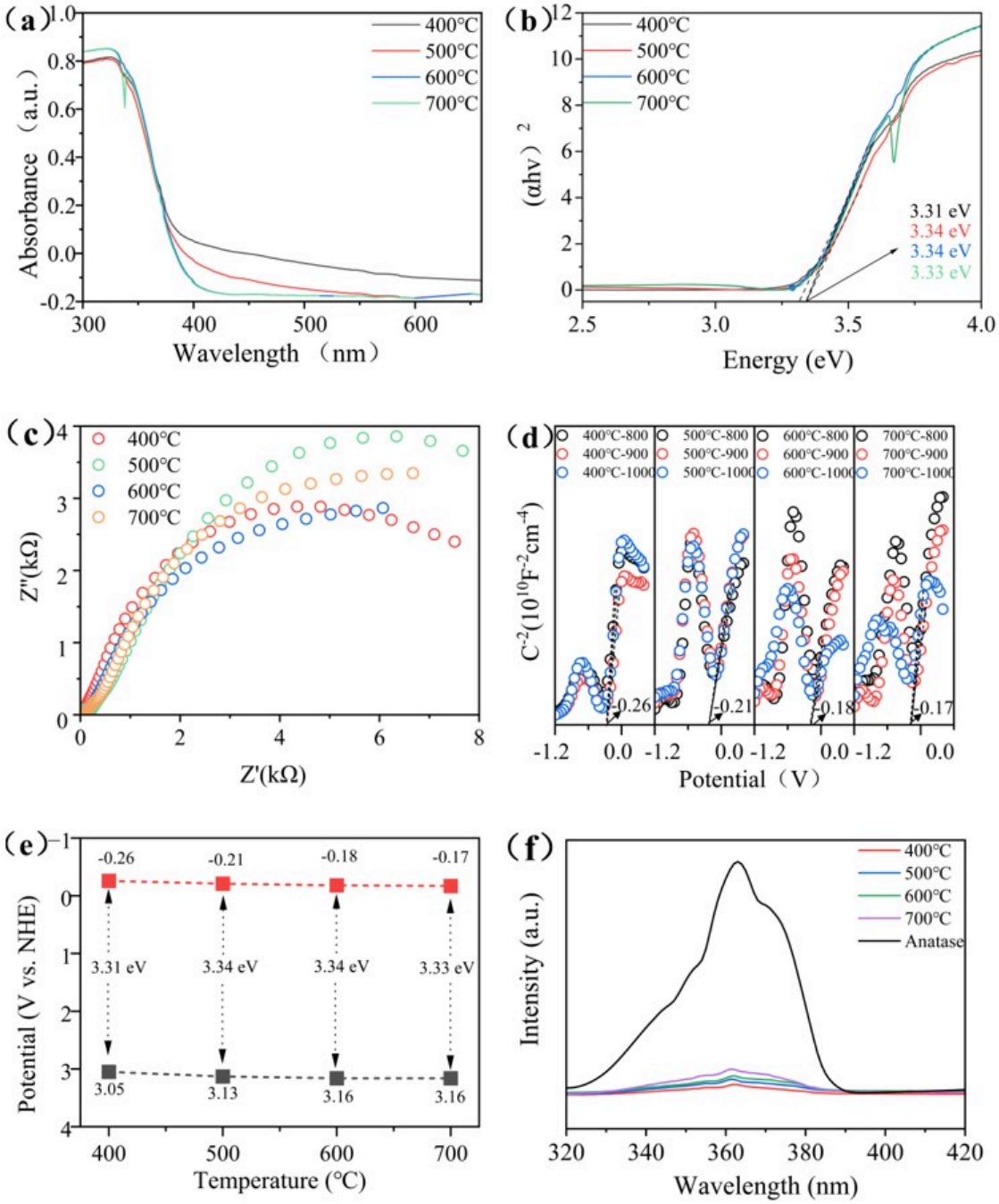



**Figure 2**

(a) UV-Vis absorption spectra of $TiO_2$ fiber membranes. (b) Tauc plots of $TiO_2$ fiber membranes. (c) electrochemical impedance spectra (EIS) of $TiO_2$ fiber membranes. (d) Mott-Schottky plots (MS) of $TiO_2$ fiber membranes. (e) band structure diagrams of $TiO_2$ fiber membranes. (f) PL spectra of $TiO_2$ fiber membranes and powder.

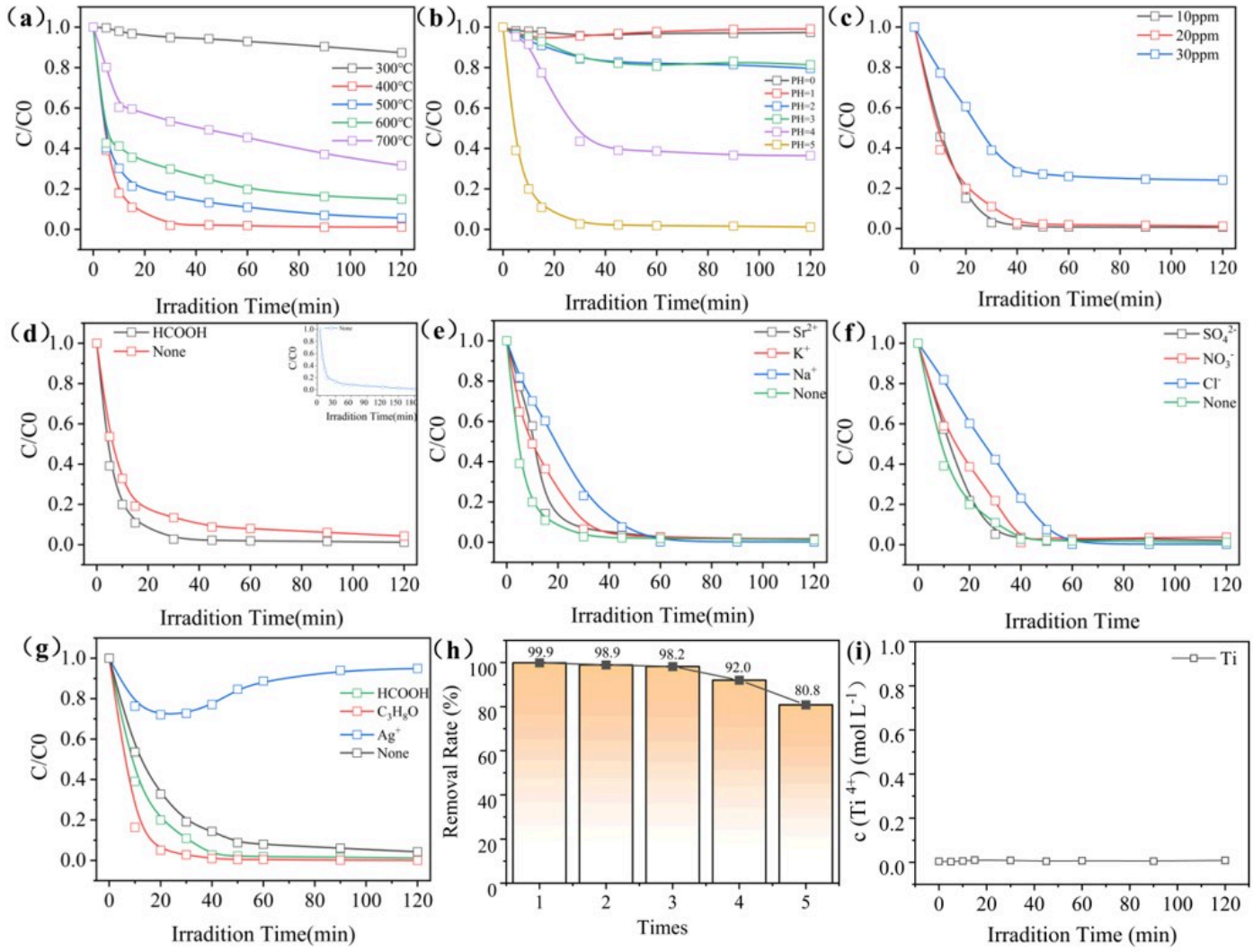



**Figure 3**

Effect of (a) thermal treatment temperature, (b) pH, (c) substrate concentration, (d) whether to added formic acid as a sacrificial agent, (e) coexisting cations, (f) coexisting anions, (g) different scavengers on $TiO_2$ fiber membranes photocatalytic reduction of U (VI), (h) Recyclability of the photocatalyst on $TiO_2$ fiber membranes photocatalytic reduction of U (VI), (i)Leaching of titanium (Ti) ions in the photocatalytic process.

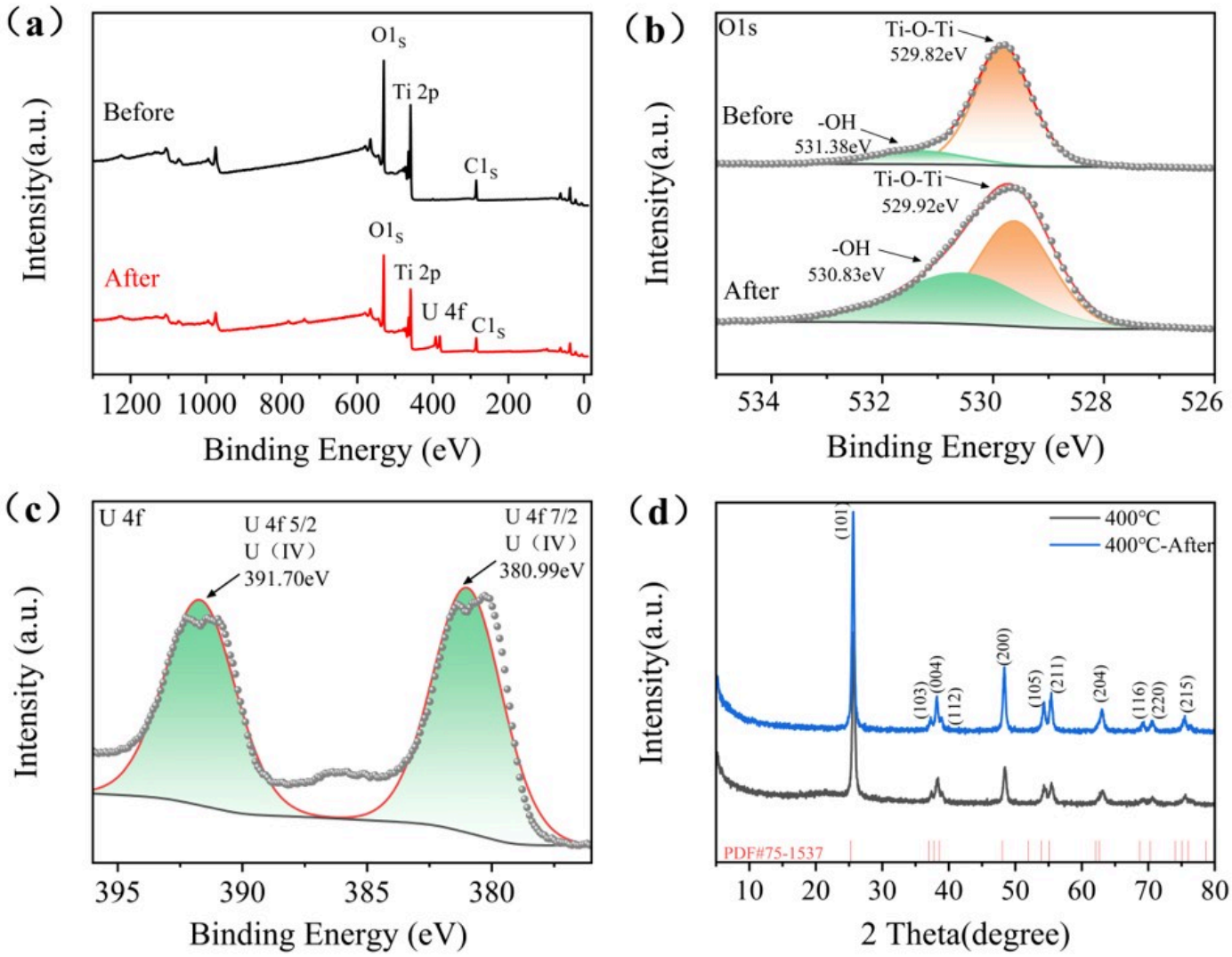



**Figure 4**

(a) XPS survey spectra of $TiO_2$ fiber membranes. (b, c) High resolution XPS spectra of O and U the corresponding characteristic peaks. (d) XRD patterns on $TiO_2$ fiber membranes.